



## A Bayesian spherical harmonics source radiation model for sound field control

**Caviedes Nozal, Diego; Heuchel, Franz Maria; Brunskog, Jonas; Riis, Nicolai Andre Brogaard; Fernandez Grande, Efen**

*Published in:*  
Journal of the Acoustical Society of America

*Link to article, DOI:*  
[10.1121/1.5133384](https://doi.org/10.1121/1.5133384)

*Publication date:*  
2019

*Document Version*  
Publisher's PDF, also known as Version of record

[Link back to DTU Orbit](#)

*Citation (APA):*  
Caviedes Nozal, D., Heuchel, F. M., Brunskog, J., Riis, N. A. B., & Fernandez Grande, E. (2019). A Bayesian spherical harmonics source radiation model for sound field control. *Journal of the Acoustical Society of America*, 146(5), 3425-3435. <https://doi.org/10.1121/1.5133384>

---

### General rights

Copyright and moral rights for the publications made accessible in the public portal are retained by the authors and/or other copyright owners and it is a condition of accessing publications that users recognise and abide by the legal requirements associated with these rights.

- Users may download and print one copy of any publication from the public portal for the purpose of private study or research.
- You may not further distribute the material or use it for any profit-making activity or commercial gain
- You may freely distribute the URL identifying the publication in the public portal

If you believe that this document breaches copyright please contact us providing details, and we will remove access to the work immediately and investigate your claim.

# A Bayesian spherical harmonics source radiation model for sound field control

Diego Cavedes-Nozal,<sup>1,a)</sup> Franz M. Heuchel,<sup>1</sup> Jonas Brunskog,<sup>1</sup> Nicolai A. B. Riis,<sup>2</sup> and Efren Fernandez-Grande<sup>1</sup>

<sup>1</sup>Acoustic Technology Group, Department of Electrical Engineering, Technical University of Denmark, Building 352, Ørstedsgade, DK-2800 Kongens Lyngby, Denmark

<sup>2</sup>Scientific Computing Group, Department of Applied Mathematics and Computer Science, Technical University of Denmark, Building 324, Richard Petersens Plads, DK-2800 Kongens Lyngby, Denmark

(Received 4 April 2019; revised 14 October 2019; accepted 21 October 2019; published online 21 November 2019)

In sound field reproduction and sound field control systems, the acoustic transfer functions between a set of sources and an extended reproduction area need to be accurately estimated in order to achieve good performance. This implies that large amounts of measurements should be performed if the area is large compared to the wavelengths of interest. In this paper, a method for reconstructing these transfer functions in highly damped conditions is proposed by using only a small number of measurements in the reproduction area. The source radiation is modeled with the spherical harmonics basis and its amplitude coefficients are fitted with Bayesian inference. This approach is validated in a sound field control experiment where a set of 12 control loudspeakers attenuate the sound pressure level generated by a set of six primary loudspeakers in a quiet zone while minimizing their radiation into a listening zone. The performance of the approach is studied by analyzing the sound field reconstruction and the sound field control performance. It is shown that it is possible to get—with few measurements and the source radiation model—results similar to those achieved using a dense grid of transfer function measurements. © 2019 Acoustical Society of America.

<https://doi.org/10.1121/1.5133384>

[JDR]

Pages: 3425–3435

## I. INTRODUCTION

Accurate knowledge of the acoustic transfer functions between a set of loudspeakers and a reproduction area is important for the implementation of multichannel reproduction systems that are used for applications in spatial sound, sound field synthesis, and sound field control. In multipoint or inverse filtering methods<sup>1,2</sup> the transfer functions, from which the loudspeaker signals are derived, must be sampled accurately and with sufficient spatial resolution to avoid aliasing effects.

Such dense spatial sampling is no issue for investigations based on simulations.<sup>3–8</sup> However, the measurement of transfer functions between multiple loudspeakers and hundreds of control points in large control areas requires large microphone arrays or many sequential measurements. Besides, placing the microphones inside the control area can also be impractical.

In order to reduce the number of measurements,<sup>9</sup> adapt transfer functions to changes in atmospheric conditions<sup>10,11</sup> or control sound at virtual sensor positions,<sup>12</sup> the sound propagation between sources and the reproduction area can be estimated using a sound propagation model. Most previous studies that used sound propagation models in a sound field control context assumed omnidirectional radiation of the sources modelled with monopoles<sup>3,13–18</sup> or a combination of monopoles and dipoles.<sup>5</sup> Such a simplification often leads to

large performance degradations when comparing the predicted and measured sound fields, e.g., a study of Chang and Jacobsen showed differences of up to 25 dB between predicted and measured acoustic contrast<sup>19</sup> due to errors in loudspeaker positioning and modelling, even though they measured the acoustic center of the loudspeakers in a separate experiment<sup>20</sup> and used a combination of monopole and dipole.

In the present study, we introduce a source radiation model for sound field control problems where the parameters of the model are fitted using *in situ* measurements. The model makes use of a spherical harmonic expansion to account for the directivity of the sources. We show that the approach enables a more accurate representation of the source radiation over large control areas compared to monopole and monopole plus dipole models of the source radiation (which are commonly found in the literature). A fair assumption in sound field control setups, where multiple loudspeakers of the same type are deployed, is to assume that all the sources share the same radiation properties. This enables us to reduce the number of model parameters, so that using the same parameter values for each source, it becomes possible to estimate these from only a handful of *in situ* measurements. Once the loudspeaker radiation properties are determined, the model can estimate transfer functions over large spatial areas. We show that these estimates are accurate enough for applications in sound zoning under anechoic conditions. The introduced method can thus considerably reduce the number of measurements needed for the setup of sound zone systems in highly damped rooms, as,

<sup>a)</sup>Electronic mail: [dicano@elektro.dtu.dk](mailto:dicano@elektro.dtu.dk)

e.g., in the aforementioned studies,<sup>7,14,19,21</sup> while maintaining a good performance. For sound field reproduction in reverberant rooms, the presented methodology might extend sound field control methods for reverberant spaces that are based on a monopole model, e.g., as proposed by Jin and Kleijn.<sup>9</sup>

There exist multiple other source radiation models and near-field reconstruction methods<sup>22–27</sup> which were developed to reconstruct the sound field in the near-field of a source, and examine their vibrational properties. The proposed spherical harmonics model is a compact representation, optimal for modeling the radiation characteristics of a compact source, as a small subset of the spherical wave functions can provide an accurate representation of the sound field radiated by the source.<sup>23</sup>

We use the Bayesian inference framework to fit the parameters of the sound propagation model to the sparsely measured transfer functions. This has been shown to be an appropriate approach for solving inverse acoustic problems and is ideally suited for combining information of physical and probabilistic natures. Antoni used Bayesian inference for reconstructing the sound field at the surface of a source finding the optimal interpolation basis.<sup>28</sup> Koyama *et al.* applied the same approach, finding the optimal driving signals of the control sources in a sound field reproduction setup assuming that the sources are omnidirectional, in a free field environment.<sup>15</sup> Other acoustic problems where the Bayesian framework has been successfully applied are acoustic source localization<sup>29–31</sup> or vibroacoustics in complex structures,<sup>32</sup> among others.

In this paper we use a hierarchical Bayesian model to find the regularization parameters and noise variance. It has been shown in previous experimental studies<sup>28,33</sup> that Bayesian inference outperforms GCV and the L-curve method for estimation of the regularization parameters in inverse acoustic problems.

The paper is structured as follows: Section II presents the methods. The sound zoning objectives are formulated to cancel the sound created by a set of primary sources in the dark zone with a set of secondary control sources, while reducing the impact of the secondary sources in the bright zone. The spherical harmonics model is presented and simplified to the geometry of the experimental setup. Bayesian inference is briefly introduced and applied to our problem. We define performance metrics to study the behavior of the applied methods in both sound field reconstruction and sound field control terms. Last, the experimental setup is described. Section III presents the analysis of results regarding model fitting, sound field reconstruction and sound field control performance. In Sec. IV we discuss further the results shown in Sec. III. Section V states the most relevant conclusions that come out of the present work.

## II. METHODS

### A. Sound zones

The objectives of the sound field control system in this paper are (1) the cancellation of sound from a primary source in a dark zone using a set of secondary control sources and (2) minimization of the sound radiated by the control sources

into a bright zone, as motivated in previous work<sup>11,34</sup> (see Figs. 1 and 2). Figure 1 shows the diagram of the signal flow in this setup. The *primary* source is fed with an unfiltered audio signal and generates the primary sound field. At a single frequency, this field is represented by the transfer function vectors  $\mathbf{h}_B \in \mathbb{C}^{N_B}$  and  $\mathbf{h}_D \in \mathbb{C}^{N_D}$  to  $N_B$  and  $N_D$  positions in the bright and dark zones, respectively. Each of the  $N_c$  *control* loudspeakers is driven by a separate control signal. Their transfer functions are represented by the transfer matrices  $\mathbf{H}_B \in \mathbb{C}^{N_B \times N_c}$  and  $\mathbf{H}_D \in \mathbb{C}^{N_D \times N_c}$  in bright and dark zones, respectively. The control signals are realized by filtering of the audio signal with the control weights  $\mathbf{w} \in \mathbb{C}^{N_c}$ . The control weights are found by the PM-ACC method,<sup>5,7,19</sup> i.e., by solving

$$\underset{\mathbf{w}}{\text{minimize}} \quad \kappa \|\mathbf{H}_B \mathbf{w}\|_2^2 + (1 - \kappa) \|\mathbf{H}_D \mathbf{w} + \mathbf{h}_D\|_2^2, \quad (1)$$

where  $\|\cdot\|_2$  is the Euclidean norm and  $\kappa \in [0, 1]$  is weighting between the two objective terms. This cost function minimizes the radiation of the control sources into the bright zone (first term) and the total sound energy of primary and control sources in the dark zone (second term). Equation (1) is a linear least squares problem and can thus be solved efficiently. Notice that we have reversed the notion of bright and dark zone here in comparison to the standard sound zoning nomenclature: the system is reproducing a target field  $-\mathbf{h}_D$  in the dark zone and minimizing the energy of the control sources in the bright zone. However, sanity is recovered when superimposing the sound fields of primary and control sources.

The solutions of the optimization problem (1) for all relevant frequencies are the complex control gains of the secondary sources  $\mathbf{w}$ . The discrete Fourier transform of the frequency domain gains is a set of real, optimal finite impulse response (FIR) filters. The control source driving signals are obtained through convolution of the audio signal with the corresponding optimal filters.

### B. Source radiation model

In this work, we model the radiation properties of the sources (directional response and sensitivity) used in the sound zoning setup. Spherical harmonics have been shown to be a useful basis for modeling<sup>35</sup> and designing<sup>13</sup> the acoustic radiation of sources. The transfer function between the midpoint of the loudspeaker box and a measurement point  $\mathbf{r} = (r, \theta, \phi)$  is<sup>36</sup>

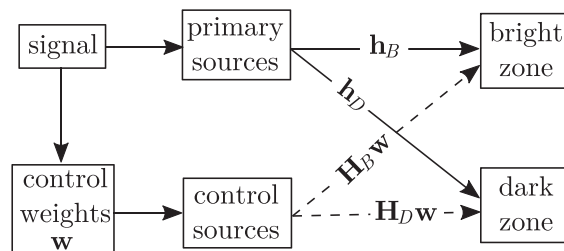


FIG. 1. Signal path diagram. The total sound field in the bright zone is  $\mathbf{H}_B \mathbf{w} + \mathbf{h}_B$ . The equivalent applies to the dark zone.

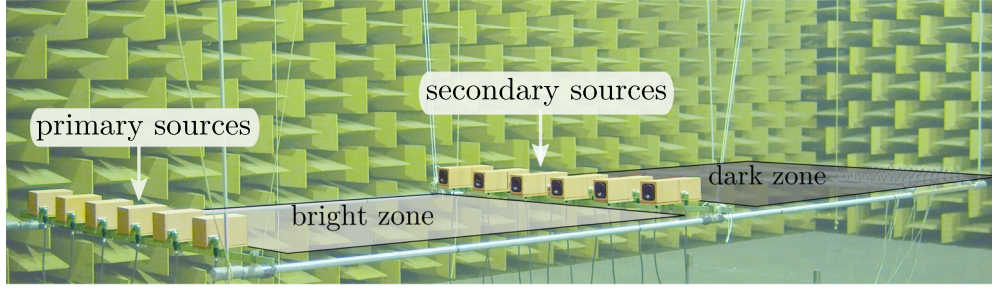


FIG. 2. (Color online) Measurement setup in anechoic chamber.

$$\hat{h}(k, \mathbf{r}) = \sum_{m=0}^{\infty} \sum_{n=-m}^m a_{mn} h_m^{(2)}(kr) Y_m^n(\theta, \phi), \quad (2)$$

where  $\theta$  is the polar angle,  $\phi$  the azimuth angle,  $k$  is the wavenumber,  $r$  is the radial distance,  $h_m^{(2)}$  are the spherical Hankel functions of the second kind,  $a_m \in \mathbb{C}$  are the coefficients of the spherical harmonics basis and

$$Y_m^n(\theta, \phi) = \sqrt{\frac{(2n+1)(m-n)!}{4\pi(m+n)!}} P_m^n(\cos(\theta)) e^{jm\phi} \quad (3)$$

are the spherical harmonics of mode order  $m$  and degree  $n$ . The terms  $P_m^n$  are the Legendre polynomials. The geometry of the setup (see Figs. 2 and 3) simplifies the formulation, and symmetry around the polar axis ( $n=0$ ) is assumed.<sup>37</sup> With this simplification,

$$\hat{h}(k, \mathbf{r}) \simeq \sum_{m=0}^M a_m h_m^{(2)}(kr) P_m(\cos(\theta)), \quad (4)$$

where the sum has been truncated to  $M$  elements.

### C. Bayesian inference and inversion

Given no transducer mismatch between neither the loudspeakers nor the microphones, it can be assumed that all the transfer functions between  $N_L$  loudspeakers and  $N_M$  measurement points are described by the same model. Thus, the recorded transfer functions per frequency  $\mathbf{h} \in \mathbb{C}^{N_L N_M}$  are modeled as  $\mathbf{h} = \hat{\mathbf{h}} + \mathbf{n}$ , where  $\mathbf{n}$  is additive noise and  $\hat{\mathbf{h}}$  is Eq. (4) in vector form

$$\hat{\mathbf{h}} = \mathbf{S}\mathbf{a}, \quad (5)$$

with  $\hat{\mathbf{h}} \in \mathbb{C}^{N_L N_M}$ ,  $\mathbf{a} \in \mathbb{C}^{M+1}$ , and  $\mathbf{S} \in \mathbb{C}^{N_L N_M \times (M+1)}$  with elements  $s_{mi} = h_m^{(2)}(kr_i) P_m(\cos(\theta_i))$ .

To calculate the unknown parameters  $\mathbf{a}$  we use Bayesian inference, which is the process of fitting a probability model to a set of data and summarizing the result by a probability distribution on the parameters of the model, called the posterior distribution.<sup>38</sup> Given a set of measured transfer functions  $\mathbf{h}$  the posterior distribution  $\pi(\mathbf{a} | \mathbf{h})$  of the parameters  $\mathbf{a}$  is the result of the Bayes' theorem

$$\pi(\mathbf{a} | \mathbf{h}) = \frac{\pi(\mathbf{h} | \mathbf{a}) \pi(\mathbf{a})}{\pi(\mathbf{h})}, \quad (6)$$

where  $\pi$  stands for probability density function.

The prior  $\pi(\mathbf{a})$  expresses our beliefs about the unknown parameters  $\mathbf{a}$  prior to the measurement of  $\mathbf{h}$ . The likelihood function  $\pi(\mathbf{h} | \mathbf{a})$  expresses the likelihood of measurement outcomes given a specific realization of the unknown parameters  $\mathbf{a}$ . The evidence  $\pi(\mathbf{h})$  is the marginal distribution of the data. In short, the posterior expresses what we know about  $\mathbf{a}$  after the measurement of a specific realization  $\mathbf{h}$ . When sampling the posterior, the evidence can be omitted as it is independent of the model parameters  $\mathbf{a}$ .

### D. Likelihood, prior, and MAP

The noise  $\mathbf{n}$  is considered complex normal (which is the maximum entropy assignment when the only information about the noise is that its variance is finite<sup>39</sup>) and circularly symmetric,<sup>40</sup> with both real and imaginary parts independent and identically normally distributed, simplifying to  $\mathbf{n} \sim \mathcal{CN}(0, \tau^{-1} \mathbf{I})$ ,  $\mathbf{I}$  being the identity matrix. This assumption is an approximation of the spatial covariance of the noise, leading to the following normally distributed likelihood:

$$\pi(\mathbf{h} | \mathbf{a}, \tau) \sim \mathcal{CN}(\hat{\mathbf{h}}, \tau^{-1} \mathbf{I}) \propto \exp(-\tau^2 \|\mathbf{S}\mathbf{a} - \mathbf{h}\|^2). \quad (7)$$

Common prior distributions for the coefficients in this type of regressions are uniform distributions and normal distributions. The uniform distribution leads to a closed analytic solution of the posterior distribution.<sup>41</sup> When a normal distribution is used, it is necessary to know both precision of noise and precision of  $\mathbf{a}$  to have an analytic solution.<sup>33,42</sup> We assume that the amplitude coefficients are normally distributed with zero mean, i.e.,  $\mathbf{a} \sim \mathcal{CN}(0, \delta^{-1} \mathbf{I})$ . This regularizes the problem as the normal distribution penalizes large coefficients. Neither of the precision hyperparameters  $\tau$  and  $\delta$  are known, and their prior distributions  $\pi(\tau)$  and  $\pi(\delta)$  are considered gamma distributions

$$\tau \sim \mathcal{G}(\alpha, \beta), \quad \delta \sim \mathcal{G}(\alpha, \beta), \quad (8)$$

which fulfill the requirement that  $\tau^{-1}, \delta^{-1} > 0$ .

The posterior distribution is proportional to the prior times the likelihood

$$\pi(\mathbf{a}, \tau, \delta | \mathbf{h}) \propto \pi(\mathbf{h} | \mathbf{a}, \tau) \pi(\mathbf{a} | \delta) \pi(\tau) \pi(\delta). \quad (9)$$

Equation (9) does not have an analytic solution.

The transfer functions can be estimated using the maximum *a posteriori* probability estimate (MAP) of Eq. (9):

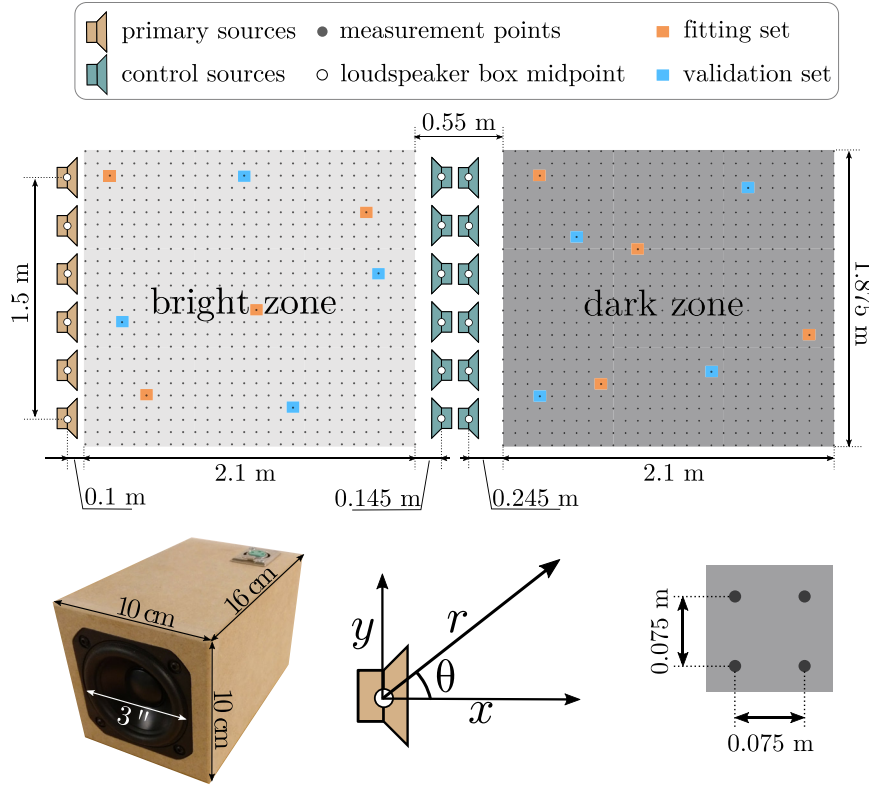


FIG. 3. (Color online) Setup geometry. Brown loudspeakers are the primary sources and blue loudspeakers the secondary control sources. White dots are the loudspeakers box midpoints. Black dots are the  $N_B + N_D = 1400$  measurement positions. Orange and blue squares are one LHS realization of the picked measurement positions used to fit and validate the model, respectively for  $N_Z = 4$ . Bottom left corner: one loudspeaker unit. Bottom center: coordinate system of the spherical harmonics model. Bottom right corner: detail of the distance between measurement points.

$$(\mathbf{a}, \tau, \delta)_{\text{MAP}} = \underset{\mathbf{a}, \tau, \delta}{\operatorname{argmax}} \pi(\mathbf{a}, \tau, \delta | \mathbf{h}). \quad (10)$$

The predicted transfer function from a source to any point  $\mathbf{r}_* = (r_*, \theta_*)$  is

$$\hat{h}(k, \mathbf{r}_*) = \mathbf{s}_* \mathbf{a}_{\text{MAP}}, \quad (11)$$

where the elements of  $\mathbf{s}_*$  are  $s_{m*} = h_m^{(2)}(kr_*) P_m(\cos(\theta_*))$ . To find the MAP estimates we use the limited-memory Broyden–Fletcher–Goldfarb–Shanno (L-BFGS) optimization algorithm included in the STAN statistical modeling package,<sup>43</sup> which has superlinear convergence and is suitable for high dimensional non-linear problems, yet making moderate use of memory resources. Other methods could otherwise be used, such as expectation maximization.<sup>44</sup>

## E. Performance metrics

We define the error between the estimated [Eq. (11)] and measured transfer functions at each frequency with the normalized mean square error<sup>45</sup>

$$\text{NMSE} = \frac{1}{N_* N_L} \sum_{i=1}^{N_*} \sum_{j=1}^{N_L} \frac{|H_{ij} - \hat{H}_{ij}|^2}{|H_{ij}|^2}. \quad (12)$$

The NMSE indicates how well the model is estimating the transfer functions on average over all loudspeaker-measurement point combinations for  $N_* \geq N_M$ . Normalizing each term in the sum separately assures that points with low and high transfer function magnitude contribute equally to the error estimate.

The insertion loss<sup>11</sup>

$$\text{IL} = 10 \log \left( \frac{\|\mathbf{h}_D\|^2}{\|\mathbf{H}_D \mathbf{w} + \mathbf{h}_D\|^2} \right) \quad (13)$$

is used to quantify the performance of the sound zone system in the dark zone, where it represents the average reduction of sound pressure level when the control sources are active.

## F. Experimental setup

The methods regarding transfer function reconstruction and sound zoning were tested in an anechoic sound zone setup as shown in Figs. 2 and 3. The equal sized bright and dark zones were separated by the control source array consisting of twelve sources (i.e.,  $N_c = 12$ ) arranged as two layers of six loudspeakers facing opposite directions. The primary source to the left hand side of the bright zone was a  $N_p = 6$  element loudspeaker array. All the  $N_L = N_p + N_c = 18$  loudspeakers were of the same type with Tymphany PLS-P830986 3-in. driver units mounted on custom made fiberboard boxes (see bottom of Fig. 3). The transfer functions of each speaker to each zone were measured with the exponential sine sweeps technique<sup>46</sup> at a dense grid of  $N_B = N_D = 700$  measurement positions per zone ( $25 \times 28$  grid of points on a plane) using a  $6 \times 10$  array of 1/4-inch microphones spaced 7.5 cm apart (black dots in Fig. 3). The sampling rate is 8192 Hz, the frequency range studied is 100–1000 Hz, the frequency resolution is 33.3 Hz and no averaging is applied. The SNR is above 20 dB in the studied frequency range. The measured temperature during the experiment was  $T = 19.4^\circ\text{C}$ . The origin of the coordinate

system for the spherical harmonics model is the loudspeaker box midpoint as specified in Fig. 3.

### III. RESULTS

In the first part of this section, the sound propagation model parameters are inferred from small, randomly chosen sets of transfer function measurements and the sound field reconstruction quality is assessed in terms of the NMSE by comparison with the densely sampled measured sound field. The radiation properties of the sources and how the model is able to incorporate them are also investigated and linked to the resulting sound field reconstruction error. Next, sound zones with the transfer functions estimated by the sound propagation model are created and the sound field control performance is studied in terms of the achieved insertion loss.

The parameter  $\kappa = 0.1$  is used to solve Eq. (1), giving more importance to the reduction of sound level in the dark zone. The prior distributions were chosen to be weakly informative,  $\alpha = 1, \beta = 10^{-2}$ . They assert no strong prior knowledge about neither the measurement error nor the spherical harmonics coefficients **a**.

#### A. Model fitting and sound field reconstruction

In each zone 50 random “fitting sets” of  $N_Z = 1, 4, 16$ , or 64 measurement positions per zone (i.e.,  $N_M = 2N_Z$ ) are picked from the entire data set via Latin hypercube sampling (LHS) in order to cover homogeneously the controlled area.<sup>47</sup> Figure 3 shows an example LHS realization for  $N_Z = 4$ . We fitted the sound propagation model and computed the performance indices for each of these realizations individually.

Figure 4 shows the average and worst case NMSE [Eq. (12)] of the 50 LHS realizations as a function of the number of measurements per zone  $N_Z$  and the truncation of the series  $M$ . The NMSE is calculated between the reconstructed and the measured transfer functions from all  $N_L = 18$  loudspeaker to the dense grid of  $N_* = N_B + N_D = 1400$  measurement positions.

As a general trend, Fig. 4 shows that more modes and more measurement positions lead to lower error, while higher frequencies show higher error. However, this trend is not followed in all cases. When  $M = 0$ , the error is equal for all  $N_Z$ , where only four parameters are inferred ( $\tau, \delta$ , and real and imaginary parts of  $a_0$ ). Even using the least number of measurement positions per zone  $N_Z = 1$ , the amount of transfer functions is already  $2N_L$  due to individual contribution of each loudspeaker, which leads to an overdetermined problem. Up to  $M = 3$  and for any  $N_Z$ , the model fitting procedure is robust to the random measurement positions picked by the Latin hypercube sampling, showing small differences between the worst case error and the average error.

Using higher order modes do not always lead to a better reconstruction. The error can increase at lower frequencies if the number of measurements is small and the number of modes is large [see Figs. 4(a) and 4(b)]. This is the result of a combination of factors: First, the spherical Neumann functions, that are part of the spherical Hankel functions of the second kind, are singular at  $kr = 0$ , which translates to a high

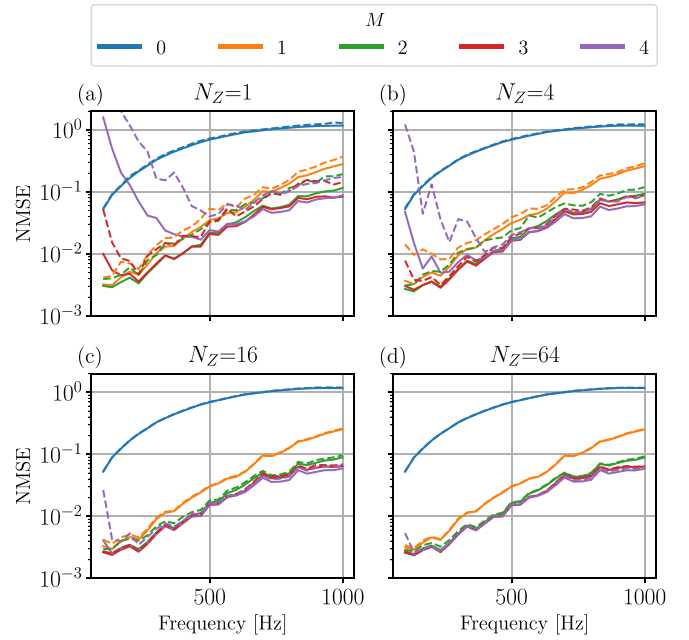


FIG. 4. (Color online) Average and worst case NMSE from 50 iterations of LHS for  $N_Z = 1, 4, 16, 64$  measurements positions per zone and  $M = 0, 1, 2, 3, 4$  truncation number in Eq. (4). (—): Average. (---): Worst case (highest NMSE).

condition number  $\kappa(\mathbf{S}^T \mathbf{S})$  and therefore to an ill-conditioned problem in Eq. (7) (see Fig. 5). Second, less data per inferred parameter is available. Last, the use of more measurement positions will give a better representation of the sound field in the whole reproduction area, both close and further away from the sources.

Figures 6 and 7 show the average spatial reconstruction error of the 50 LHS realizations at 133 and 700 Hz, respectively. The error is calculated for different truncation numbers (from top to down in the figure,  $M = 0, 1$ , and 4) and different number of measurement positions per zone (from left to right,  $N_Z = 1$  and 4), using Eq. (12) without summing over the dimension  $i$  (i.e., measurement positions). As it was shown in Fig. 4, a monopole ( $M = 0$ ) is a poor representation of the sources, presenting errors between  $(-10, -6)$  dB and  $(-0.5, 1)$  dB at 133 Hz (Fig. 6, top row) and 700 Hz (Fig. 7, top row), respectively, in both zones. A higher number of measurements per zone ( $N_Z = 4$ ) when  $M = 0$  does not improve the reconstruction significantly, agreeing with the results in Fig. 4.

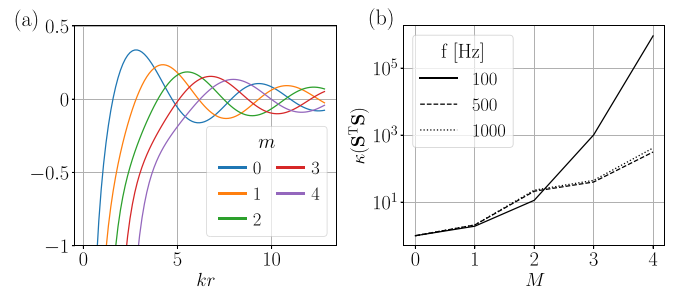


FIG. 5. (Color online) (a) Spherical Neumann function. (b) Average condition number  $\kappa(\mathbf{S}^T \mathbf{S})$  for all LHS realizations of  $N_Z = 1$ .

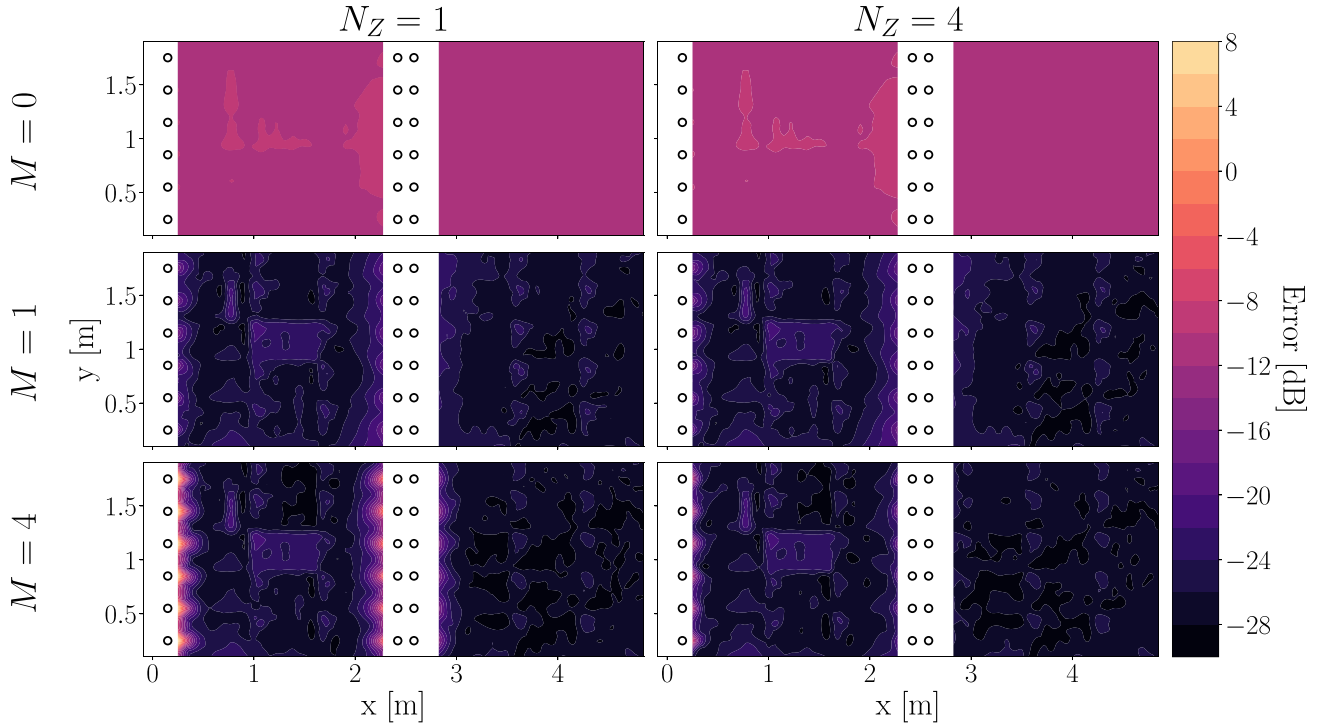


FIG. 6. (Color online) Spatial error at 133 Hz of the reconstructed transfer functions  $[(1/N_L) \sum_{j=1}^{N_L} (|H_j - \hat{H}_j|^2) / (|H_j|^2)]$ , for different truncation number in the spherical harmonics model ( $M = 0, 1$ , and  $4$ ) and number of measurement positions per zone ( $N_Z = 1$  and  $4$ ).

Increasing the truncation to  $M = 1$  (i.e., monopole plus dipole) leads to a dramatic increase of the reconstruction accuracy at 133 Hz, with errors below -15 dB in the entire reconstructed areas (Fig. 6, middle row). This is due to the fact that the radiation properties of the sources can be accounted for with the higher order terms. At 700 Hz the reconstruction is also improved compared to  $M = 0$ , with errors up to -4 dB next to the sources (Fig. 7, middle row). The error shows a well defined spatial pattern consequence of the poor agreement between the source directional model and the actual loudspeaker behavior.

When the truncation number is increased to  $M = 4$ , the directional response at 700 Hz is well modeled and the reconstruction error drops below -5.5 dB in both zones (Fig. 7, bottom row). At 133 Hz (Fig. 6, bottom row) the reconstruction error is similar to that achieved when  $M = 1$ , but there is an increase in the error close to the sources when the number of measurements per zone is  $N_Z = 1$ , with values up to 8 dB. This is due to the ill-conditioning of the problem in Eq. (7) when the number of modes is high and the number of measurements low (see Fig. 5). Increasing the number of measurements per zone to  $N_Z = 4$  reduces this error in the vicinity of the sources, which is aligned with the results shown in Figs. 4(a) and 4(b).

Artifacts in the form of vertical lines approximately 70 cm apart can be appreciated at low errors for  $M = 1$  and  $M = 4$ , especially at higher frequencies (Fig. 7). The reason is an imperfect calibration of the microphone array due to its positioning.

Figure 8 presents the normalized marginal posterior distributions,  $\pi(\mathbf{a}|\mathbf{h})$ , of the first two modes [Fig. 8(a)], the normalized MAP amplitude of the different modes [Fig. 8(b)]

and the estimated directional response of the sources at different frequencies at 1 m [Fig. 8(c)]. At higher frequencies the loudspeaker becomes more directional [Fig. 8(c)] and higher order modes play a significant role [Fig. 8(b)]. This is the reason why, as shown in Figs. 4, 6, and 7, the error is reduced at higher frequencies when adding higher order modes to the sum, showing that a simple monopole representation ( $M = 0$ ) is not sufficient for accurate reconstruction of the radiation of these sources.

The marginal posterior distributions in Fig. 8(a) show a larger variance for higher frequencies. This is due to an increasing discrepancy between the model and the measurements, a low amount of measurements relative to the wavelength and the lower relevance of lower modes at higher frequencies [see Fig. 8(b)].

## B. Sound field control performance

The insertion loss obtained using the estimated transfer functions at the entire dense grid of points in Fig. 2 is compared with the reference insertion loss obtained using the actual measured transfer functions at the same grid of points. The estimated transfer functions correspond to the same estimated transfer functions used to calculate the error in Fig. 4. In both measured and estimated cases, half of the transfer functions are used to calculate the control weights  $\mathbf{w}$  and the other half to calculate the resulting insertion loss. Figure 9 shows the amplitude of the resulting transfer functions ( $\mathbf{h}_D + \mathbf{H}_D \mathbf{w}$  and  $\mathbf{h}_B + \mathbf{H}_B \mathbf{w}$ ) at 700 Hz for the measured reference case and an example using the estimated transfer functions for  $M = 4$ ,  $N_Z = 16$ .

Figure 10 shows the average and worst case insertion loss of the 50 LHS realizations as a function of the number

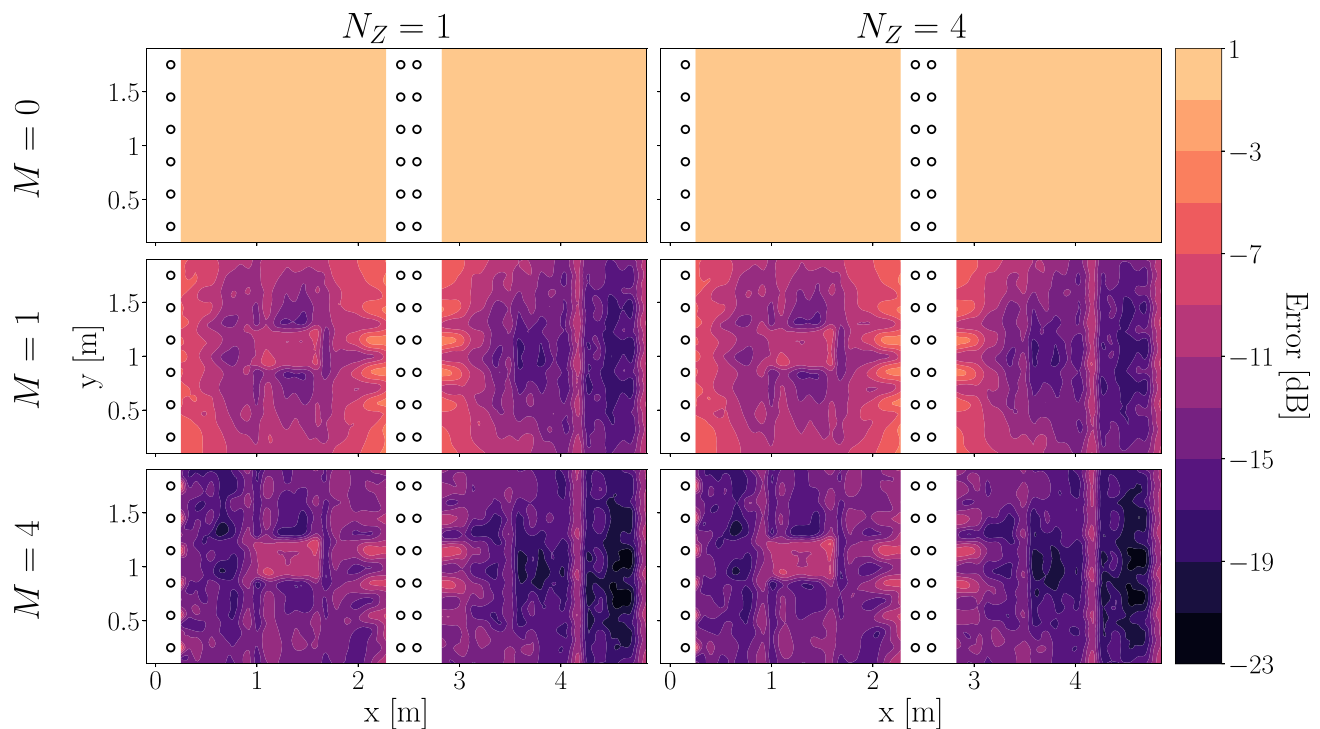


FIG. 7. (Color online) Spatial error at 700 Hz of the reconstructed transfer functions  $[(1/N_L) \sum_{j=1}^{N_L} (|H_j - \hat{H}_j|^2) / (|H_j|^2)]$ , for different truncation number in the spherical harmonics model ( $M = 0, 1$ , and  $4$ ) and number of measurement positions per zone ( $N_Z = 1$  and  $4$ ).

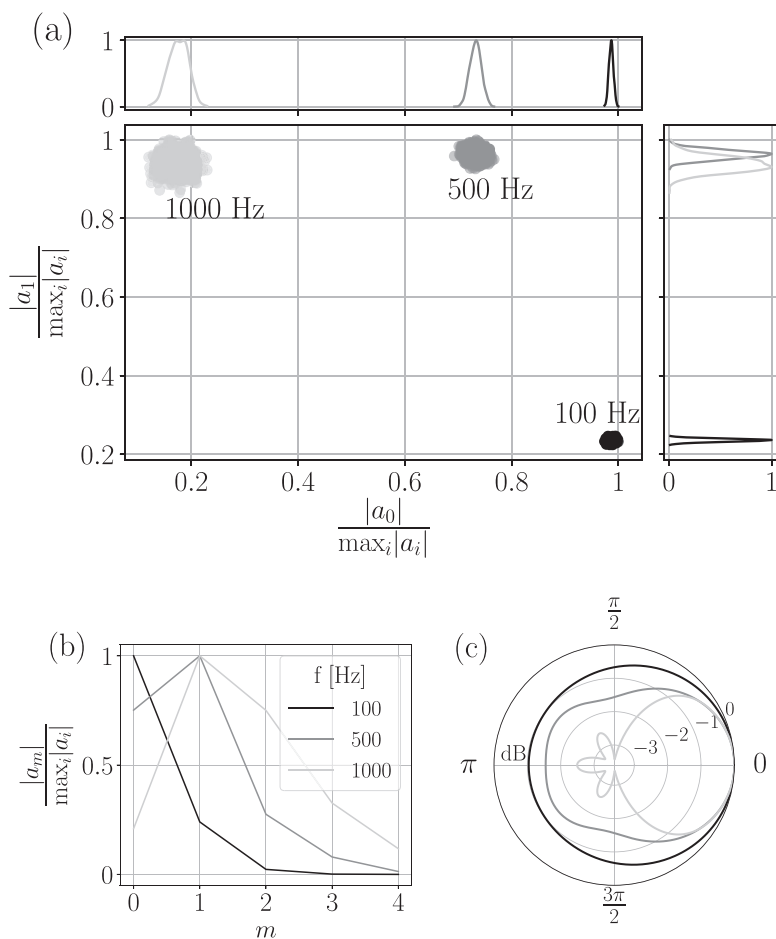


FIG. 8. Marginal posterior distribution,  $\pi(\mathbf{a}|\mathbf{h})$ , of the amplitude coefficients  $a_m$  for the first two modes, calculated MAP amplitude coefficients  $\mathbf{a}$  and estimated directional response at 1 m for  $N_Z = 16$ . (a) Posterior joint and marginal distributions of the normalized amplitudes of the first two modes  $[|a_0|/\max_i(|a_i|)]$  and  $[|a_1|/\max_i(|a_i|)]$ . (b) MAP normalized amplitude  $|a_m|/\max_i(|a_i|)$  up to  $m=4$  for 100, 500, and 1000 Hz. (c) Estimated directional response of the loudspeakers at 1 m for 100, 500, and 1000 Hz in dB summing all the modes up to  $M=4$ .

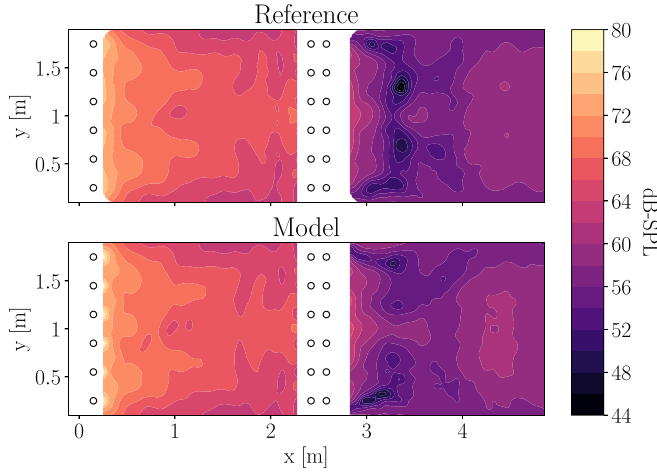


FIG. 9. (Color online) Resulting transfer function field at 700 Hz. Top: Reference result using half of the measured transfer functions. Bottom: using the model with  $M = 4$ ,  $N_Z = 16$ .

of measurements per zone  $N_Z$  and the modes included  $M$ . The obtained insertion loss is directly related to the reconstruction error of the transfer functions shown in Fig. 4. The average insertion loss is equal to the reference measured insertion loss (black line in the figure) at low frequencies for all cases except  $M = 0$ . At higher frequencies the inclusion of more modes in the model increases the insertion loss, although it is not possible to get as high values as using the measured transfer functions. Increasing the number of measurement points slightly improves the insertion loss on average, but it noticeably reduces the difference between worst case and average results especially at low frequencies. Figure 10 clearly shows that a good sound zoning solution is

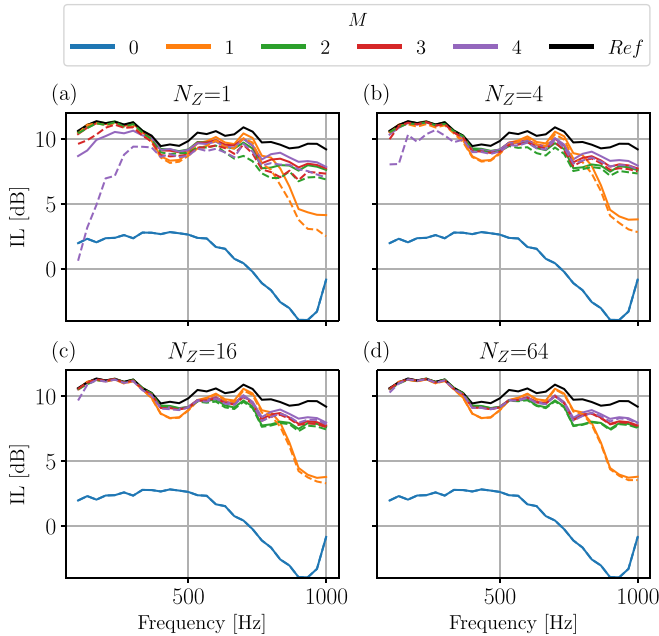


FIG. 10. (Color online) Average and worst case insertion loss from 50 iterations of LHS for  $N_Z = 1, 4, 16$ , and  $64$  measurements positions per zone and  $M = 0, 1, 2, 3$ , and  $4$  truncation number in Eq. (4). (—): Average. (---): Worst case (lowest IL). Ref: IL using half of the dense grid of measured transfer functions in Fig. 3 ( $N_Z = 350$ ).

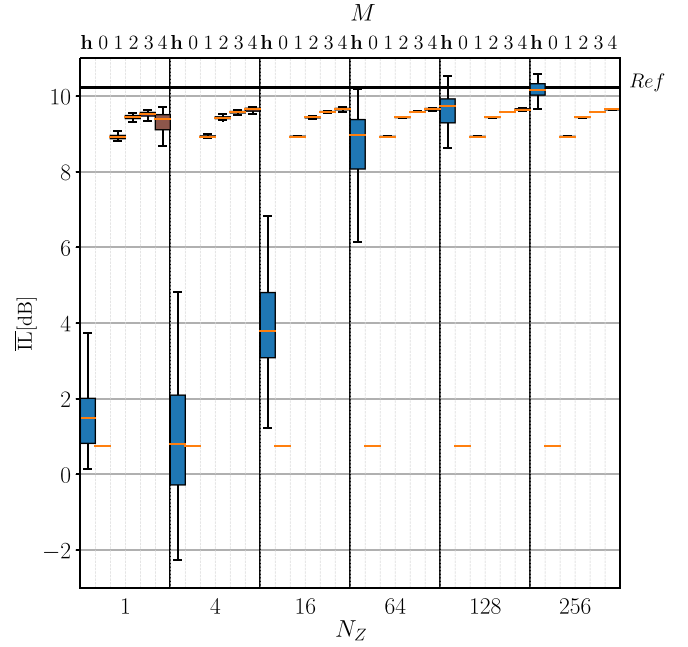


FIG. 11. (Color online) Insertion loss averaged over the studied frequency range from 100 to 1000 Hz ( $\overline{IL}$ ). The box plots show the median in orange and the boxes extend from first to third quartile. The whiskers represent the extreme cases (max and min). Bottom  $x$  axis: Number of measurement positions per zone  $N_Z$ . Top  $x$  axis: Truncation number in the spherical harmonics basis  $M$ . **h**: No model used. **Ref**: Insertion loss using half of the dense grid of measured transfer functions in Fig. 3 ( $N_Z = 350$ ).

achievable with a small number of measurement points and the use of a sound propagation model.

The insertion loss achieved using the reconstructed transfer functions (see Fig. 10) is compared with the insertion loss achieved if the control filters are calculated directly from the sparse measured data points  $N_M = 2N_Z$ . Figure 11 shows the frequency averaged insertion loss  $\overline{IL}$  for the 50 LHS for both approaches, where the columns labeled **h** refer to the insertion loss achieved when the control filters are calculated directly from the sparse measurements. To see the trend of the estimated insertion loss with larger number of measurements we include two extra cases  $N_Z = 128$  and  $256$ .

Using the reconstructed transfer functions, the insertion loss increases by increasing the number of modes for a given  $N_Z$ , with  $\overline{IL} > 7.5$  dB for any case where  $M > 1$ . The variance between realizations is reduced when increasing the number of measurements. Many more measurements are needed to achieve similar insertion loss when the control weights are calculated directly from the sparse measurement positions. The performance is always below the  $\overline{IL}$  obtained with the reconstructed transfer functions for  $N_Z = 1$ ,  $M = 2$  up to  $N_Z = 64$  and it is not until  $N_Z \geq 128$  when using the reconstructed transfer functions shows a worse performance. This clearly shows the advantage of reconstructing the transfer functions using the model if the number of measurements is small.

The fact that the maximum  $\overline{IL}$  for  $N_Z \geq 128$  without using the model is higher than the reference ( $N_Z = 350$ ) is due to the effect of  $\kappa$  in Eq. (1). For some of the cases, very high IL can be achieved while the sound field in the bright zone gets distorted.

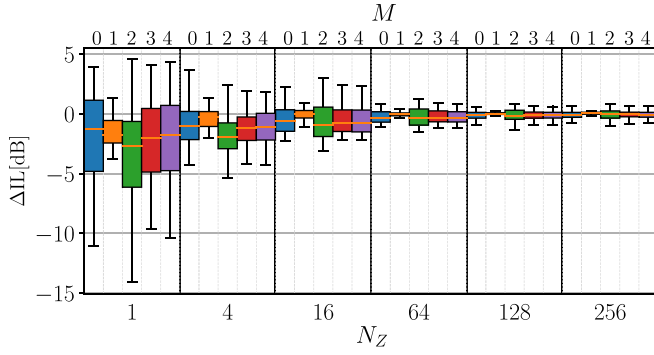


FIG. 12. (Color online) Frequency averaged IL difference  $\Delta IL = \overline{IL} - \overline{IL}_{val}$  of the 50 LHS. The box plots show the median in orange and the boxes extend from first to third quartile. The whiskers represent the extreme cases (max and min). Bottom x axis: Number of measurement positions per zone  $N_Z$ . Top x axis: Truncation number in the spherical harmonics basis  $M$ .

### C. Insertion loss at sparse measurement points

The results shown in Secs. III A and III B are a consequence of comparing the reconstructed transfer functions with the measured transfer functions at a dense grid of points. In practice, this would imply measuring hundreds of transfer functions what is indeed what we are trying to avoid.

The insertion loss at a few validation points is compared to the insertion loss in the entire zone. Figure 12 shows the frequency averaged insertion loss difference  $\Delta IL = \overline{IL} - \overline{IL}_{val}$  where  $\overline{IL}_{val}$  is the insertion loss at 50 LHS sets of  $N_Z = 1, 4, 16, 64$ , and  $256$  validation positions, independent from the fitting positions (see Fig. 3), and  $IL$  is the insertion loss using half of the measured transfer functions ( $N_Z = 350$ ). It can be observed that using a low number of validation points the insertion loss is overestimated with deviations up to 15 dB when  $N_Z = 1$ . Including more validation points,  $\overline{IL}_{val}$  gets closer to the insertion loss at the entire controlled zone. For all cases the lowest and more stable  $\Delta IL$  corresponds to  $M = 1$ .

## IV. DISCUSSION

The insertion loss obtained using the reconstructed transfer functions is lower than the insertion loss achieved using a dense grid of measured transfer functions, which can imply that there is room for improvement. The only parameters fitted in the acoustic model in Eq. (4) are the complex amplitudes of the modes. There are other factors that highly influence the estimation of the transfer functions, such as temperature<sup>11,12</sup> and positions of individual microphones and loudspeakers.<sup>15,34,48</sup> These positions could be estimated as well if necessary, even though more measurements would be needed to fit these additional parameters.

The loudspeaker response is influenced by the arrangement of the array,<sup>20</sup> which suggests that independent models for primary and secondary arrays could improve the reconstruction. In addition there are some acoustic phenomena happening in the experiment that are not captured by the model. The secondary sources introduce scattering effects in the sound field created by the primary sources. If the loudspeaker box were a sphere of equal volume (i.e., radius

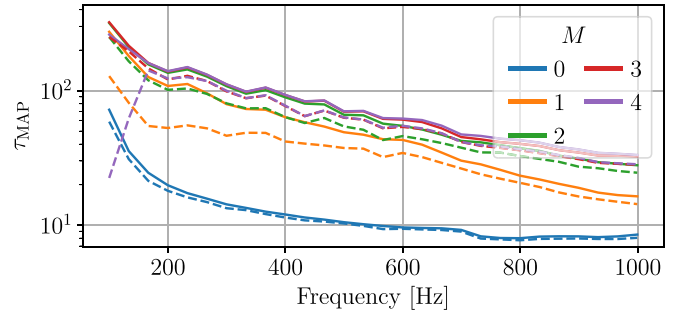


FIG. 13. (Color online) Average and worst case MAP of  $\tau$  from 50 iterations of LHS for  $N_Z = 16$  measurement positions per zone and truncation number  $M = 0, 1, 2, 3$ , and  $4$  in the sum. (—): Average. (---): Worst case.

$b \simeq 7$  cm), it would be noticeable above  $kb = 1$  affecting frequencies above approximately 750 Hz.<sup>37</sup>

The difference between model and reality, also called model discrepancy, can severely affect the resulting marginal posterior of the variance of the noise, as  $\tau$  will capture both measurement noise and model discrepancy.<sup>49</sup> Fig. 13 shows how the noise precision increases when the model discrepancy is reduced (i.e., when more modes are used). This effect can be attenuated with a good prior estimation of the measurement noise and either setting  $\tau$  as a fixed parameter or considering a more informative prior.

We assume that the measurements are affected by independent noise of equal variance. However, it is possible to include more complex sources of noise, such as external background noise with spatial correlation between measurements in the covariance matrix.

In previous works the sources were modeled as point sources with a complex directivity<sup>50</sup> or as a combination of monopole plus dipole,<sup>5</sup> where the acoustic center needs to be found in a different measurement setup. Using spherical harmonics the model is fitted *in situ* and there is no need for determining the acoustic center of the sources precisely. The error of choosing a wrong center for the spherical harmonics is on average compensated by adding more modes. Figure 8 shows how at 100 Hz and 1 m the loudspeaker behaves as an omnidirectional source moved to the front, compensating for the assumption of having the acoustic sources located at the mid points of the loudspeakers boxes.

A more informative prior of the parameters  $\mathbf{a}$  can be used to counter the ill-posedness introduced by high order modes at low frequencies, reducing the number of measurements to converge. This requires more precise *a priori* information about the amplitude coefficients.

Low number of validation points tends to overestimate the achieved insertion loss in the entire controlled area according to Fig. 12. Techniques like optimal experiment design could be used together with the proposed model, to decide in which positions the transfer functions should be measured in order to get the best experimental conditions.<sup>51</sup> This could potentially reduce the number of measurements needed both to fit the model and validate the sound field control performance.

We applied the sound propagation model and the fitting of its parameters with Bayesian inference to the problem of

sound zones, but these methods can be employed for any highly damped problem where transfer function have to be reconstructed over a large area.

## V. CONCLUSIONS

A spherical harmonics model has been proposed to characterize the sound radiation of loudspeakers and reconstruct the acoustic transfer functions in multichannel reproduction systems based on multipoint or inverse filtering methods. The approach was experimentally validated in a rectangular sound field control setup of 10 m<sup>2</sup> at the frequency range [100–1000] Hz under anechoic conditions.

The results show that reconstructing the transfer functions with the proposed model can substantially improve the performance of the system. The frequency averaged insertion loss obtained using the reconstructed sound field with the model from a few sparse measurements positions per zone is always above the insertion loss obtained using the same amount of measurements without the model, with improvements up to 10 dB or more. The introduced method considerably reduces the number of measurements needed to have a good performance of the sound field control system. Furthermore, the results indicate that a simple monopole or monopole plus dipole model, as often assumed in the literature, is not sufficient to model the radiation of the loudspeakers. Including higher order modes in the spherical harmonics basis allows us to capture high frequency phenomena and the directivity of the sources, improving the reproduction performance.

## ACKNOWLEDGMENTS

We would like to thank Finn T. Agerkvist for all the valuable input and Henrik Hvidberg for the technical support. This work is part of the MONICA project and has received funding from the European Union's Horizon 2020 research and innovation program under grant agreement No 732350.

- <sup>1</sup>T. Betlehem, W. Zhang, M. A. Poletti, and T. D. Abhayapala, "Personal sound zones: Delivering interface-free audio to multiple listeners," *IEEE Signal Process. Mag.* **32**(2), 81–91 (2015).
- <sup>2</sup>W. Zhang, P. N. Samarasinghe, H. Chen, and T. D. Abhayapala, "Surround by sound: A review of spatial audio recording and reproduction," *Appl. Sci.* **7**(5), 1–19 (2017).
- <sup>3</sup>J.-W. Choi and Y.-H. Kim, "Generation of an acoustically bright zone with an illuminated region using multiple sources," *J. Acoust. Soc. Am.* **111**(4), 1695–1700 (2002).
- <sup>4</sup>M. Poletti, "An investigation of 2-D multizone surround sound systems," in *Proceedings of the 125th AES International Convention*, San Francisco (October 2–5, 2008).
- <sup>5</sup>J.-H. Chang and F. Jacobsen, "Sound field control with a circular double-layer array of loudspeakers," *J. Acoust. Soc. Am.* **131**(6), 4518–4525 (2012).
- <sup>6</sup>Y. J. Wu and T. D. Abhayapala, "Spatial multizone soundfield reproduction: Theory and design," *IEEE Trans. Audio, Speech, Lang. Process.* **19**(6), 1711–1720 (2011).
- <sup>7</sup>M. B. Møller, M. Olsen, and F. Jacobsen, "A hybrid method combining synthesis of a sound field and control of acoustic contrast," in *Proceedings in the AES 132nd International Convention*, Budapest, Hungary (April 26–29, 2012).
- <sup>8</sup>M. A. Poletti and T. D. Abhayapala, "Interior and exterior sound field control using general two-dimensional first-order sources," *J. Acoust. Soc. Am.* **129**(1), 234–244 (2011).

- <sup>9</sup>W. Jin and W. B. Kleijn, "Theory and design of multizone soundfield reproduction using sparse methods," *IEEE/ACM Trans. Audio, Speech, Lang. Process.* **23**(12), 2343–2355 (2015).
- <sup>10</sup>M. Olsen and M. B. Møller, "Sound zones: On the effect of ambient temperature variations in feed-forward systems," in *Audio Engineering Society Convention 142*, Audio Engineering Society (2017).
- <sup>11</sup>F. M. Heuchel, D. Caviedes Nozal, F. T. Agerkvist, and J. Brunskog, "Sound field control for reduction of noise from outdoor concerts," in *the 145th AES International Convention*, New York City (October 17–20, 2018), pp. 1–8.
- <sup>12</sup>M. B. Møller and M. Olsen, "Sound zones: On performance prediction of contrast control methods," in *Proceedings of the 2016 AES International Conference on Sound Field Control*, Guildford, UK (July 18–20, 2016).
- <sup>13</sup>M. A. Poletti, F. M. Fazi, and P. A. Nelson, "Sound reproduction systems using variable-directivity loudspeakers," *J. Acoust. Soc. Am.* **129**(3), 1429–1438 (2011).
- <sup>14</sup>F. Jacobsen, M. Olsen, M. Møller, and F. T. Agerkvist, "A comparison of two strategies for generating sound zones in a room," in *Proceedings of the 18th International Congress on Sound and Vibration International Institute of Acoustics and Vibration*, Rio de Janeiro, Brazil (July 10–14, 2011).
- <sup>15</sup>S. Koyama, K. Furuya, Y. Haneda, and H. Saruwatari, "Source-location-informed sound field recording and reproduction," *IEEE J. Sel. Top. Signal Process.* **9**(5), 881–894 (2015).
- <sup>16</sup>T. Okamoto and A. Sakaguchi, "Experimental validation of spatial Fourier transform-based multiple sound zone generation with a linear loudspeaker array," *J. Acoust. Soc. Am.* **141**(3), 1769–1780 (2017).
- <sup>17</sup>S. J. Elliott, J. Cheer, J.-W. Choi, and Y. Kim, "Robustness and regularization of personal audio systems," *IEEE Trans. Audio, Speech, Lang. Process.* **20**(7), 2123–2133 (2012).
- <sup>18</sup>Q. Zhu, P. Coleman, M. Wu, and J. Yang, "Robust acoustic contrast control with reduced in-situ measurement by acoustic modeling," *J. Audio Eng. Soc.* **65**(6), 460–473 (2017).
- <sup>19</sup>J.-H. Chang and F. Jacobsen, "Experimental validation of sound field control with a circular double-layer array of loudspeakers," *J. Acoust. Soc. Am.* **133**(4), 2046–2054 (2013).
- <sup>20</sup>J. H. Chang, J. Jensen, and F. Agerkvist, "Shift of the acoustic center of a closed-box loudspeaker in a linear array: Investigation using the beam-forming technique," *J. Audio Eng. Soc.* **63**(4), 257–266 (2015).
- <sup>21</sup>J.-H. Chang, C.-H. Lee, J.-Y. Park, and Y.-H. Kim, "A realization of sound focused personal audio system using acoustic contrast control," *J. Acoust. Soc. Am.* **125**(4), 2091–2097 (2009).
- <sup>22</sup>J. D. Maynard, E. G. Williams, and Y. Lee, "Nearfield acoustic holography: I. Theory of generalized holography and the development of NAH," *J. Acoust. Soc. Am.* **78**(4), 1395–1413 (1985).
- <sup>23</sup>J. Hald, "Basic theory and properties of statistically optimized near-field acoustical holography," *J. Acoust. Soc. Am.* **125**(4), 2105–2120 (2009).
- <sup>24</sup>M. R. Bai, "Application of BEM (boundary element method)-based acoustic holography to radiation analysis of sound sources with arbitrarily shaped geometries," *J. Acoust. Soc. Am.* **92**(1), 533–549 (1992).
- <sup>25</sup>Z. Wang and S. F. Wu, "Helmholtz equation-least-squares method for reconstructing the acoustic pressure field," *J. Acoust. Soc. Am.* **102**(4), 2020–2032 (1997).
- <sup>26</sup>A. Sarkissian, "Method of superposition applied to patch near-field acoustic holography," *J. Acoust. Soc. Am.* **118**(2), 671–678 (2005).
- <sup>27</sup>E. Fernandez-Grande, A. Xenaki, and P. Gerstoft, "A sparse equivalent source method for near-field acoustic holography," *J. Acoust. Soc. Am.* **141**(1), 532–542 (2017).
- <sup>28</sup>J. Antoni, "A Bayesian approach to sound source reconstruction: Optimal basis, regularization, and focusing," *J. Acoust. Soc. Am.* **131**, 2873–2890 (2012).
- <sup>29</sup>E. Zhang, J. Antoni, B. Dong, and H. Snoussi, "Bayesian space-frequency separation of wide-band sound sources by a hierarchical approach," *J. Acoust. Soc. Am.* **132**(5), 3240–3250 (2012).
- <sup>30</sup>W. T. Kung, Y. Y. Lee, and H. Y. Sun, "Sound leakage identification for an enclosed room using the probabilistic approach and model class selection index: An experiment," *J. Sound Vib.* **310**(4–5), 776–781 (2008).
- <sup>31</sup>A. Xenaki, E. Fernandez-Grande, and P. Gerstoft, "Block-sparse beam-forming for spatially extended sources in a Bayesian formulation," *J. Acoust. Soc. Am.* **140**(3), 1828–1838 (2016).
- <sup>32</sup>M. Sadri, J. Brunskog, and D. Younesian, "Application of a Bayesian algorithm for the Statistical Energy model updating of a railway coach," *Appl. Acoust.* **112**, 84–107 (2016).
- <sup>33</sup>A. Pereira, J. Antoni, and Q. Leclère, "Empirical Bayesian regularization of the inverse acoustic problem," *Appl. Acoust.* **97**, 11–29 (2015).

- <sup>34</sup>F. M. Heuchel, D. Caviedes Nozal, J. Brunskog, E. F. Grande, and F. T. Agerkvist, "An adaptive, data driven sound field control strategy for outdoor concerts," in *Proceedings of the 3rd AES International Conference on Sound Reinforcement—Open Air Venues*, Struer, Denmark (August 30–September 2, 2017).
- <sup>35</sup>W.-H. Cho, "Sound source modelling and synthesis by the equivalent source method for reproducing the spatial radiation characteristics," in *Proceedings of the 2016 AES International Conference on Sound Field Control*, Guildford, UK (July 18–20, 2016).
- <sup>36</sup>E. G. Williams, "Spherical waves," in *Fourier Acoustics: Sound Radiation and Nearfield Acoustical Holography* (Elsevier, New York, 1999), Chap. 6.
- <sup>37</sup>F. Jacobsen and P. Juhl, "Sound radiation and scattering," in *Fundamentals of General Linear Acoustics*, 1st ed. (Wiley, New York, 2013), Chap. 9, pp. 187–202.
- <sup>38</sup>A. Gelman, J. B. Carlin, H. S. Stern, D. B. Dunson, A. Vehtari, and D. B. Rubin, "Probability and inference," in *Bayesian Data Analysis*, 3rd ed. (Chapman and Hall, Boca Raton, FL, 2013), Chap. 1, pp. 1–25.
- <sup>39</sup>D. Dowson and A. Wragg, "Maximum-entropy distributions having prescribed first and second moments," *IEEE Trans. Inf. Theory* **19**(5), 689–693 (1973).
- <sup>40</sup>R. G. Gallager, "Random processes and noise," in *Principles of Digital Communication* (Cambridge University Press, Cambridge, 2008), Chap. 7, pp. 227–232.
- <sup>41</sup>J. Escolano, N. Xiang, J. M. Perez-Lorenzo, M. Cobos, and J. J. Lopez, "A Bayesian direction-of-arrival model for an undetermined number of sources using a two-microphone array," *J. Acoust. Soc. Am.* **135**(2), 742–753 (2014).
- <sup>42</sup>J. M. Bardsley, "Markov chain Monte Carlo methods for linear inverse problems," in *Computational Uncertainty Quantification for Inverse Problems*, 1st ed. (SIAM, Philadelphia, PA, 2018), Chap. 5.
- <sup>43</sup>Stan, "Stan modeling language user's guide and reference manual," *User's Manual Version 2.18.0* (2018).
- <sup>44</sup>C. M. Bishop, "The EM algorithm in general," in *Pattern recognition and machine learning*, 1st ed. (Springer, New York, 2006), Chap. 9.4.
- <sup>45</sup>S. A. Verburg and E. Fernandez-Grande, "Reconstruction of the sound field in a room using compressive sensing," *J. Acoust. Soc. Am.* **143**(6), 3770–3779 (2018).
- <sup>46</sup>S. Müller and P. Massarani, "Transfer-function measurement with sweeps," *J. Audio Eng. Soc.* **49**(6), 443–471 (2001).
- <sup>47</sup>W.-L. Loh, "On Latin hypercube sampling," *Ann. Stat.* **24**(5), 2058–2080 (1996).
- <sup>48</sup>S. J. Elliott and M. Jones, "An active headrest for personal audio minimally radiating sources for personal audio," *J. Acoust. Soc. Am.* **119**(5), 2702–2709 (2006).
- <sup>49</sup>J. Brynjarsdóttir and A. O'Hagan, "Learning about physical parameters: The importance of model discrepancy," *Inverse Probl.* **30**(11), 114007 (2014).
- <sup>50</sup>D. Caviedes Nozal and J. Brunskog, "Parameter optimization of forward sound propagation models using Bayesian inference," in *Proceedings of Euronoise 2018*, Crete, Greece (May 27–31, 2018), pp. 2301–2308.
- <sup>51</sup>J. Berger, D. Dutykh, and N. Mendes, "On the optimal experiment design for heat and moisture parameter estimation," *Exp. Therm. Fluid Sci.* **81**, 109–122 (2017).